Electromagnetic diffraction of light focused through a planar interface between materials of mismatched refractive indices: structure of the electromagnetic field. I

P. Török*

Department of Materials, University of Oxford, Oxford OX1 3PH, UK

P. Varga

Central Research Institute for Physics of the Hungarian Academy of Sciences, Research Institute for Materials Science, Budapest, P.O. Box 49, H-1525, Hungary

G. R. Booker

Department of Materials, University of Oxford, Oxford OX1 3PH, UK

Received December 7, 1994; revised manuscript received May 5, 1995; accepted May 10, 1995

We consider the diffraction occurring when light is focused by a lens without spherical aberration through a planar interface between materials of mismatched refractive indices, which focusing produces spherical aberration. By means of a rigorous vectorial electromagnetic treatment that was previously developed for this problem [Török *et al.,* J. Opt. Soc. Am. A **12,** 325 (1995)], the diffraction integrals are transformed into a form that is computable. Time-averaged electric energy density distributions in the region of the focused probe are numerically evaluated for air–glass and air–silicon interfaces as a function of lens numerical aperture and probe depth corresponding to a wide range of spherical aberration. Two-dimensional lateral $(x-y)$ and meridional $(x-z)$ electric energy density plots show how the energy, the size, and the position of the various axial and lateral maxima changed, providing new information concerning the above two important optical systems. The treatment also shows that the use of a lens without spherical aberration to focus into a second material is formally equivalent to the use of a lens with spherical aberration and a reduced solid semi-angle to focus into a single material.

1. INTRODUCTION

In a previous paper[1] we obtained a rigorous analytical solution for the vectorial electromagnetic diffraction occurring when light was focused by a high-aperture lens through an interface between materials of mismatched refractive indices. The interface was planar and perpendicular to the optical axis, and the two materials were homogeneous and isotropic. It was shown for such a system that the focusing produces spherical aberration and that the aberration could be described by a closed analytical function. Furthermore, the diffraction integrals obtained were in forms that were considered to be readily computable because each of the three main diffraction integrals consisted of only a single integral. The aim of the present work is to show that these integrals can be numerically evaluated and to obtain results for the time-averaged electric energy density distributions for this system corresponding to a wide range of lens apertures and probe depths and for different materials.

We initially describe previous work that used numerical computations for diffraction associated with focusing by a high-aperture lens into a single homogeneous and isotropic material with no aberrations present. The basis of many of the numerical results is due to Wolf,[2] who solved the diffraction problem by using the representation of angular spectrum of plane waves, the solution obtained being formally identical to the Debye integral. Richards and Wolf[3] computed electric energy density distributions in the focal plane of a lens for different apertures and determined the polarization states. Boivin and Wolf[4] computed the two-dimensional structure of the time-averaged electric energy density in 0° and 45° meridional planes of a high-aperture focusing system, where 0° indicates the direction of incident polarization, and showed that the lateral resolution (based on the width of the main energy density maximum) was superior in the 90° meridional plane than in the 0° plane. Hardy and Treves[5] applied Wolf's theory to stigmatic lenses, taking into account the curvature of the lens surface and the polarization-dependent effect of transmission on this surface. They computed contours of time-averaged electric and magnetic energy density with a particular lens solid semi-angle and showed that both the distributions in the focal plane were elliptical in shape.

We now describe previous work that used numerical computations for diffraction associated with a focusing system when aberrations were present. Hopkins and Yzuel[6] considered focusing by a lens into a single material. They used the Kirchhoff theory with lens aber-

0740-3232/95/102136-09$06.00

ration (measured as the distance between the reference sphere and the aberrated wave front), devised a numerical method to evaluate their integrals, and computed intensity axial line scans for weak spherical aberration. They showed how spherical aberration distorted the distribution and shifted the axial focus position. Kant[7] showed how lens aberrations could be incorporated into Wolf's theory[2] and obtained solutions for the cases of spherical aberration, curvature of field, and distortion. He computed electric energy density distributions in the best receiving plane when the first two aberrations were present and obtained values for the focus shift as a function of lens solid semiaperture. Ling and Lee[8] considered a system in which the aberration was introduced by focusing through an interface into a material with a different refractive index and solved the diffraction problem by using the angular spectrum representation. They presented time-averaged electric energy density distributions in the focal plane and also along the 0° meridional plane for weak spherical aberration and determined focus shifts and considered the effect of materials with various refractive indices on intensity maxima. However, they used a semigeometrical optics approach and an approximation to evaluate their integrals.

Most of the previous computed results for energy distributions were given as one-dimensional line scans or two-dimensional contour plots and showed the positions and the energy densities of the various axial and lateral maxima and minima in the region of the focused probe. The present results are given as two-dimensional contour plots and two-dimensional gray-scale images. The new aspects of the present work are the use of a rigorous vectorial theory, the focusing into two materials of practical importance, and the consideration of a wide range of focusing conditions corresponding to a wide range of spherical aberration produced by the interface focusing.

Numerical computations of the equations obtained by either formal or analytical solution for such diffraction systems are difficult to perform because the integrals involved are strongly oscillating functions. Although procedures for treating such integrals have been proposed,[7,9] we directly computed our equations using a cluster of seven Hewlett Packard Apollo workstations. The programs were written in FORTRAN, and for integration the D01DAF NAG (Numerical Algorithm Group, Oxford) subroutine was used.

In Section 2 of this paper we summarize our previous theoretical results and transform the diffraction integrals into a form suitable for numerical computations. We present numerical results in Subsection 3.A for an air–glass interface and an illumination wavelength of $\lambda = 0.6328\ \mu$m and in Subsection 3.B for an air–silicon interface and an illumination wavelength of $\lambda = 1.3\ \mu$m. In Section 4 we discuss and summarize our results. More detailed results concerning some aspects of the work will be presented in a subsequent paper.

2. INTEGRAL REPRESENTATION

Consider an optical system of revolution with an optical axis z as shown in Fig. 1. This system images a point source, which is situated in the object space at $z = -\infty$ and radiates a linearly polarized monochromatic and coherent electromagnetic wave. The incident polarization direction is parallel to the x direction. This wave is incident on a lens of aperture Σ, which produces a convergent spherical wave in the image space. The origin O of the (x, y, z) coordinate system is positioned in the second material, where the Gaussian focus is located. The electric and magnetic fields are determined at the arbitrary point P in the focal region. The aperture size and the distance of P from the aperture are taken to be large compared with the wavelength. In Fig. 1 $\hat{s}_1 = (s_{1x}, s_{1y}, s_{1z})$ is the unit vector for a typical ray in the first material, $\hat{s}_2 = (s_{2x}, s_{2y}, s_{2z})$ is the unit vector for a ray in the second material, and $\mathbf{r}_p = (x_2, y_2, z_2)$ is the position vector pointing from O to P. The interface between the first and the second material is situated at $z = -d$. The refractive indices of the first and the second material are denoted by n_1 and n_2, respectively.

The angle of incidence at the interface is denoted by ϕ_1, and the angle of refraction is denoted by ϕ_2. The unit vectors $\hat{s}_1$ and $\hat{s}_2$ and the vector $\mathbf{r}_p$ (Fig. 1) are given in spherical polar coordinates by

$$\hat{s}_1 = (\sin\phi_1 \cos\theta)\hat{i} + (\sin\phi_1 \sin\theta)\hat{j} + (\cos\phi_1)\hat{k}, \quad (1)$$

$$\hat{s}_2 = (\sin\phi_2 \cos\theta)\hat{i} + (\sin\phi_2 \sin\theta)\hat{j} + (\cos\phi_2)\hat{k}, \quad (2)$$

$$\mathbf{r}_p = r_p[(\sin\phi_p \cos\theta_p)\hat{i} + (\sin\phi_p \sin\theta_p)\hat{j} + (\cos\phi_p)\hat{k}], \quad (3)$$

where $\hat{i}$, $\hat{j}$, and $\hat{k}$ are the unit base vectors of the (x, y, z) orthogonal system and the spherical polar coordinates r, ϕ, and θ are defined so that $r > 0$, $0 \le \phi < \pi$, and $0 \le \theta < 2\pi$.

Let $\tilde{\mathbf{E}}(P, t)$ indicate the time-dependent electric field and let $\tilde{\mathbf{H}}(P, t)$ indicate the time-dependent magnetic field at P at time t, so that

$$\tilde{\mathbf{E}}(P, t) = \mathrm{Re}[\mathbf{E}(P)\exp(-i\omega t)],$$
$$\tilde{\mathbf{H}}(P, t) = \mathrm{Re}[\mathbf{H}(P)\exp(-i\omega t)], \quad (4)$$

where Re indicates the real part.

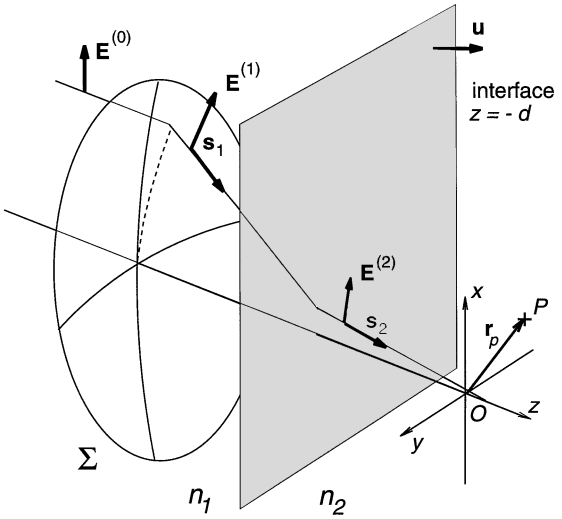

Fig. 1. Diagram showing light focused by a lens into two media separated by a planar interface.

We showed previously[1] that the Cartesian components of the electric field $\mathbf{E}_2$ inside the second material were given by a combination of the three functions

$$\begin{aligned} e_{2x} &= -iK[I_0^{(e)} + I_2^{(e)} \cos(2\theta_p)], \\ e_{2y} &= -iKI_2^{(e)} \sin(2\theta_p), \\ e_{2z} &= -2KI_1^{(e)} \cos\theta_p, \end{aligned} \tag{5}$$

where[10]

$$K = \frac{k_1 f l_0}{2} = \frac{\pi n_1 f l_0}{\lambda}$$

and

$$\begin{aligned} I_0^{(e)} &= \int_0^{\alpha} (\cos\phi_1)^{1/2} \sin\phi_1 \exp[ik_0\Psi(\phi_1, \phi_2, -d)] \\ &\quad \times (\tau_s + \tau_p \cos\phi_2) J_0\left(\frac{v \sin\phi_1}{\sin\alpha}\right) \exp\left(\frac{iu \cos\phi_2}{\sin^2\alpha}\right) \mathrm{d}\phi_1, \\ I_1^{(e)} &= \int_0^{\alpha} (\cos\phi_1)^{1/2} \sin\phi_1 \exp[ik_0\Psi(\phi_1, \phi_2, -d)] \\ &\quad \times \tau_p \sin\phi_2 J_1\left(\frac{v \sin\phi_1}{\sin\alpha}\right) \exp\left(\frac{iu \cos\phi_2}{\sin^2\alpha}\right) \mathrm{d}\phi_1, \\ I_2^{(e)} &= \int_0^{\alpha} (\cos\phi_1)^{1/2} \sin\phi_1 \exp[ik_0\Psi(\phi_1, \phi_2, -d)] \\ &\quad \times (\tau_s - \tau_p \cos\phi_2) J_2\left(\frac{v \sin\phi_1}{\sin\alpha}\right) \exp\left(\frac{iu \cos\phi_2}{\sin^2\alpha}\right) \mathrm{d}\phi_1, \end{aligned} \tag{6}$$

with ϕ_1 and ϕ_2 related by Snell's law. There was a similar set of equations for the magnetic field. It should be noted that Eqs. (5) are in a form identical to that given by Richards and Wolf[3] for a single material.

In Eqs. (6) the aberration function Ψ is

$$\Psi(\phi_1, \phi_2, -d) = -d(n_1 \cos\phi_1 - n_2 \cos\phi_2), \tag{7}$$

and the normalized radial and axial coordinates v and u, respectively, are

$$\begin{aligned} v &= k_1(x^2 + y^2)^{1/2} \sin\alpha = k_1 r_p \sin\phi_p \sin\alpha, \\ u &= k_2 z \sin^2\alpha = k_2 r_p \cos\phi_p \sin^2\alpha, \end{aligned} \tag{8}$$

where α is the solid semi-angle of the lens in the first material, k_0, k_1, and k_2 are the wave numbers *in vacuo,* in the first material, and in the second material, respectively, f is the focal length of the lens *in vacuo,* and l_0 is an amplitude factor. The standard expressions were used for the Fresnel transmission coefficients τ_s and τ_p and for the Bessel functions J_n of the first kind.

For numerical purposes it is advantageous to transform the diffraction integrals of Eqs. (6) to the second material.[11] The general form of the transformed integrals is given by

$$\begin{aligned} I_l^T(u_2, v_2) &= \frac{n_2}{n_1} \int_0^{\beta} F_l(\cos\phi_2) \exp[ik_0\Psi(\cos\phi_2)] \\ &\quad \times J_l\left(\frac{v_2 \sin\phi_2}{\sin\beta}\right) \exp\left(\frac{iu_2 \cos\phi_2}{\sin^2\beta}\right) \mathrm{d}\phi_2, \end{aligned} \tag{9}$$

where $l = 0, 1, 2$. The transformation also leads to a redefinition of the normalized coordinates:

$$\begin{aligned} v_2 &= k_2(x^2 + y^2)^{1/2} \sin\beta = k_2 r_p \sin\phi_p \sin\beta, \\ u_2 &= k_2 z \sin^2\beta = k_2 r_p \cos\phi_p \sin^2\beta, \end{aligned} \tag{10}$$

where β is the solid semi-angle in the second material corresponding to α.

Important conclusions can be drawn from Eqs. (9) and (10). It is seen from these equations that the diffraction integrals $I_l^T(u_2, v_2)$ describe the focusing of plane waves by a lens with a solid semi-angle β and with normalized optical coordinates v_2 and u_2. Hence the optical system under consideration behaves in the same way as if the focusing occurred by a reduced solid semi-angle lens ($n_1 < n_2$ and $\beta < \alpha$), and thus the effective solid semi-angle of the entire system is decreased. For example, when focusing occurs from air to glass with a lens possessing a solid semi-angle of 64.2° (numerical aperture 0.9), the resulting solid semi-angle is 36.9°. It is also clear that our optical system can be regarded as a focusing setup in which nonperfect spherical waves emerge from an aperture situated in the second material. The deviations of this imaginary (nonperfect) spherical surface from an ideal one are described by the aberration function Ψ. In our model the imaginary sphere is bounded by individual plane waves, and the distortion of the imaginary sphere can be described by the direction of the plane-wave normals. The above interpretation of Eq. (9) is inherent in the Wolf integrals, from which our integral formulas were derived, as we need to specify only the initial phase of the individual plane waves with respect to an arbitrarily chosen wave front.

Additionally, it can easily be shown that when the two exponent expressions in Eq. (9) are written in the argument of the same exponent, the equation takes a form identical to that of the original Wolf integral, where the term aberration function indicates a wave-front deviation with respect to the Gaussian reference sphere. This means that the integrand of our diffraction integrals of Eq. (9) is a combination of an aperture (apodization) function, a term (consisting of the Bessel functions) associated with lateral coordinates, and an exponential term associated with the defocus *and* the phase aberration. Thus we can consider Eq. (9) as an expression in which the effect of the aberrating second material is formally transformed into the lens and the focusing occurs into a homogeneous material by an imperfect lens.

3. NUMERICAL RESULTS

We performed numerical computations by using our diffraction integrals of Eq. (9) to determine the electric energy density distributions occurring when red or infrared light is focused through air into glass or silicon, respectively. The first case is important because focusing the light of a He–Ne laser into or through a glass layer is common practice in experimental optics. The second case is important in material science, in which examinations of semiconductor slabs and wafers by either the infrared microscope,[12] the scanning infrared microscope,[13] or the confocal scanning infrared microscope[14] are increasingly being performed.

In the following two subsections we present numerical results concerning the above two cases for the time-averaged electric energy density (referred to as electric energy density) of a lens that obeys Abbe's sine condition and for which the incident illumination is linearly polarized with a direction coinciding with the lateral x direction. The term probe depth refers to a depth below the interface (i.e., at positive z positions) at which the electric energy density is determined, i.e., is probed. For example, a probe depth of 5 μm means that the electric energy density is determined at $+5$ μm from the interface for all the positions of the interface, with respect to the lens. In particular, to plot an $x-z$ distribution, we move both the interface and the point of observation (P) along the z direction to include all axial points necessary. This consideration corresponds to the most frequent experimental case, i.e., the electric or magnetic field to be determined is probed by an object embedded in the second material, at constant depth below the interface. Axial direction refers in what follows to positive or negative directions parallel to the optical axis (z), and lateral direction refers to those directions perpendicular to the optical axis (see Fig. 1). Although the electric energy density values are given in arbitrary units, the values all correspond to a constant incident beam energy, and so the energies in all the figures in this paper can be directly compared. Axial coordinates for $x-z$ distributions are plotted so that the $z = 0$ position coincides with the paraxial focus defined by Eq. (52) of Ref. 1. When the axial location of the electric energy maximum does not coincide with the paraxial focus (which effect is due to spherical aberration), the optical distance between the paraxial focus and the energy maximum is referred to as the focus shift. In the following figures in which the focus shift needs to be considered, only the shift that is due to diffraction is included, i.e., the shift that is due to the probe depth is not.

A. Air–Glass Interface

In this subsection all numerical computations were performed for a wavelength of $\lambda = 0.6328$ μm and refractive indices of $n_1 = 1.0$ and $n_2 = 1.5$ for the first and second materials, respectively. In Figs. 2(a)–2(c) electric energy densities are shown in the $x-z$ plane for numerical apertures of (a) 0.3, (b) 0.6, and (c) 0.9, corresponding to solid semi-angles in air of 17.5°, 36.9°, and 64.2°, respectively, and in glass of 11.5°, 23.6°, and 36.9°, respectively. The probe depth is 5 μm. The energy density contours are plotted on a logarithmic scale. The results show that the electric energy becomes more concentrated as the numerical aperture increases, as expected. On going from a numerical aperture of 0.3 to 0.6, the energy density for the axial maximum increases by $\sim 15\times$, and on going from 0.3 to 0.9, it increases by $\sim 45\times$. As the numerical aperture increases, the focus shift increases but is small. For a numerical aperture of 0.3 the energy distribution is closely symmetrical about the focal plane. For a numerical aperture of 0.6 it is slightly asymmetrical, this asymmetry being more pronounced with the lateral subsidiary maxima. For a numerical aperture of 0.9 the distribution is asymmetrical, with the axial maxima being more pronounced in the positive z direction and the lateral maxima being displaced in the positive z direction. The lateral and axial FWHM's of the main electric energy maximum are substantially decreased with respect to those corresponding to numerical apertures of 0.3 and 0.6. At the negative axial di-

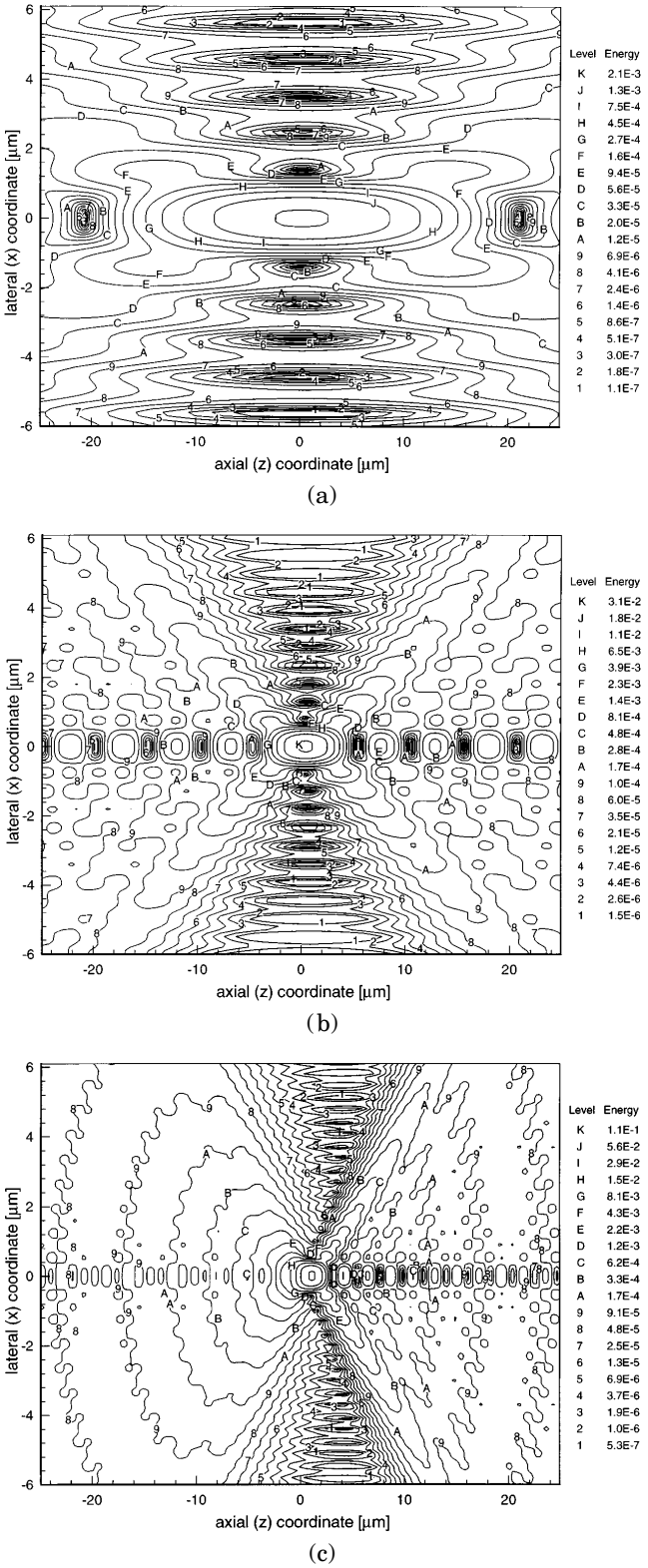

Fig. 2. Time-averaged electric energy density distributions in the $x-z$ meridional plane for a probe depth of 5 μm and for numerical apertures of (a) 0.3, (b) 0.6, and (c) 0.9. The calculations are for air ($n_1 = 1.0$) and glass ($n_2 = 1.5$) and a wavelength of $\lambda = 0.6328$ μm (He–Ne laser). 2.1E-3 is 2.1×10^{-3}, and so on, in this and subsequent figures.

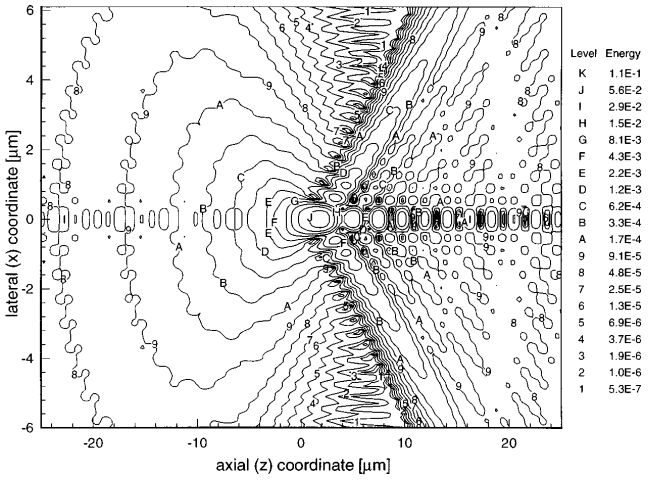

(a)

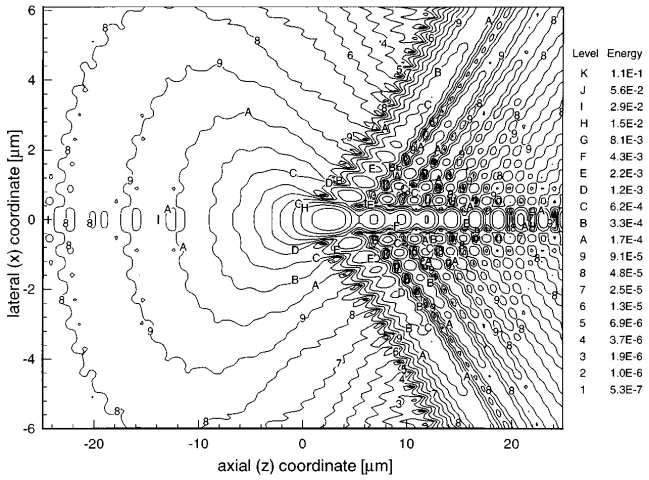

(b)

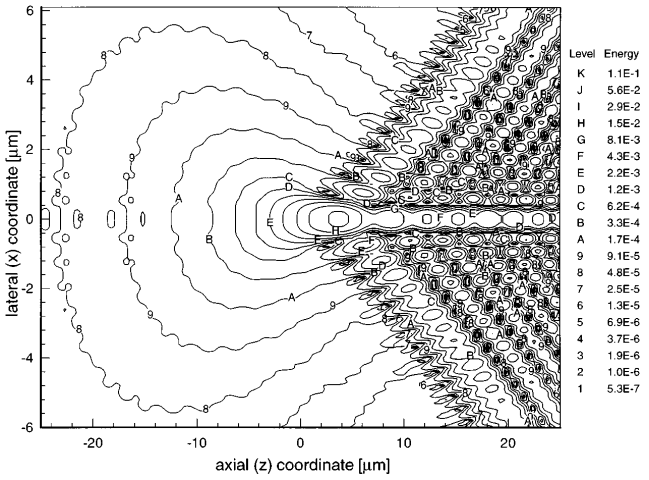

(c)

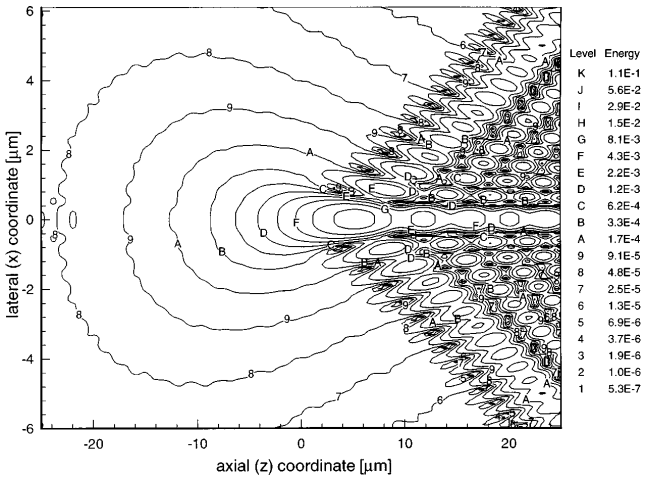

(d)

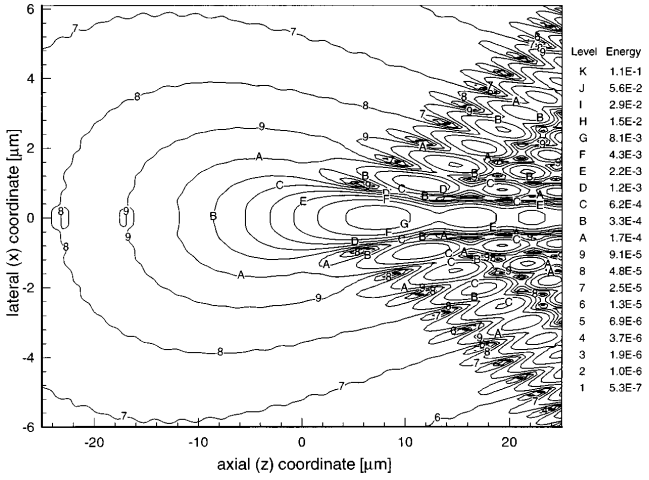

(e)

Fig. 3. Time-averaged electric energy density distributions in the $x-z$ meridional plane for a numerical aperture of 0.9 and for probe depths of (a) 10, (b) 20, (c) 40, (d) 80, and (e) 160 μm. The calculations are for air ($n_1 = 1.0$) and glass ($n_2 = 1.5$) and a wavelength of $\lambda = 0.6328$ μm (He–Ne laser).

rection local maxima become smaller in electric energy and local minima become larger; thus the modulation of subsidiary peaks at the negative axial direction becomes less pronounced compared with that at the positive axial direction.

In Figs. 3(a)–3(e) electric energy densities are shown in the $x-z$ plane for a numerical aperture of 0.9 and probe depths of (a) 10, (b) 20, (c) 40, (d) 80, and (e) 160 μm. The electric energy becomes less concentrated as the probe depth increases. On going from a depth of 5 to 160 μm, for the main maximum the energy density decreases by ~13×. The focus shift increases and is large. The axial positions of the lateral subsidiary maxima are progressively shifted toward the positive z direction, their structure becomes more complex, and their energy density increases with respect to the main maximum. It will be

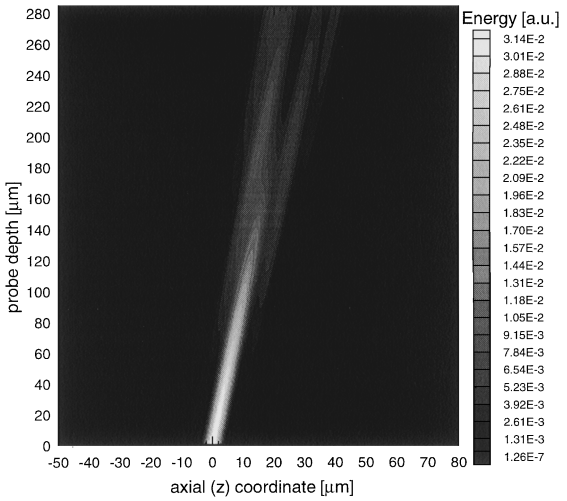

(a)

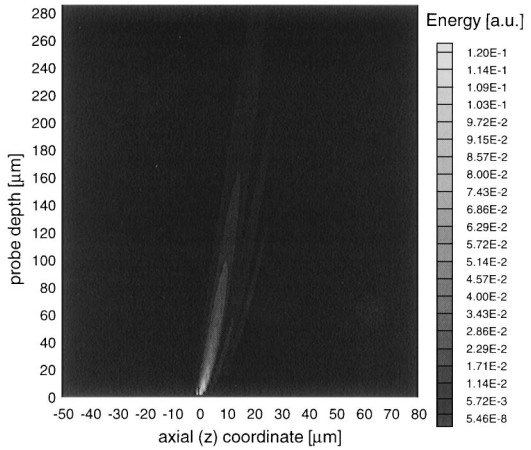

(b)

Fig. 4. Axial scans of the time-averaged electric energy density distribution for numerical apertures of (a) 0.6 and (b) 0.9 as a function of probe depth from 0 to 280 μm. The calculations are for air ($n_1 = 1.0$) and glass ($n_2 = 1.5$) and a wavelength of $\lambda = 0.6328$ μm (He–Ne laser).

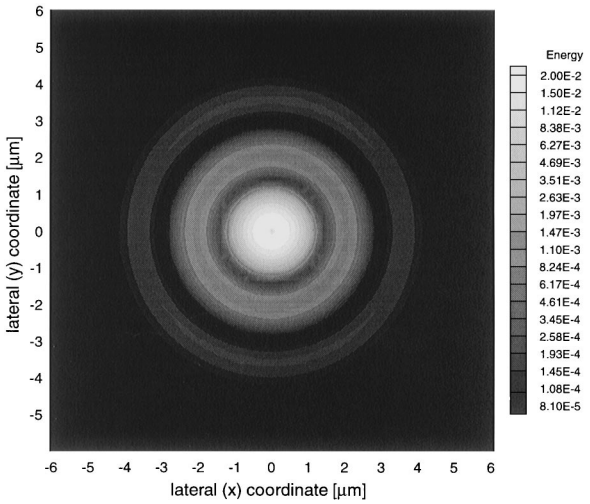

Fig. 5. Time-averaged electric energy density distributions for a numerical aperture of 0.9 in the focal $x-y$ plane when the probe depth is 160 μm. The calculations are for air ($n_1 = 1.0$) and glass ($n_2 = 1.5$) and a wavelength of $\lambda = 0.6328$ μm (He–Ne laser).

shown by direct computations in the subsequent paper that the FWHM of the main energy maximum increases with the probe depth, the effect being greater in the axial

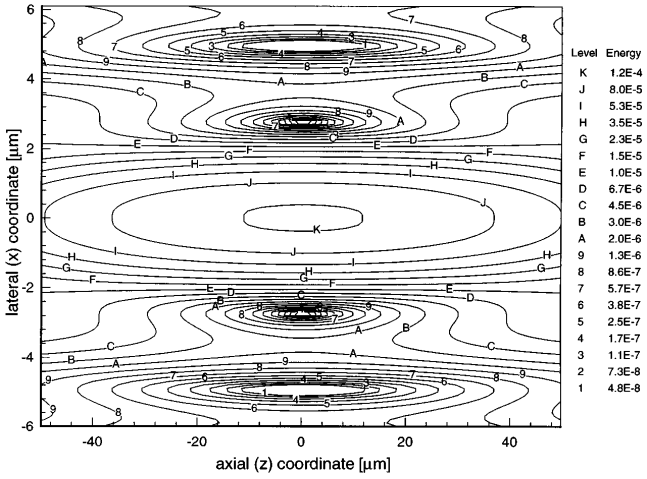

(a)

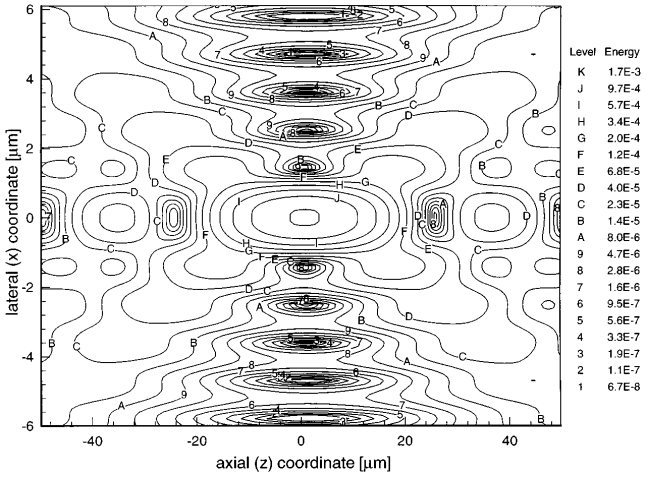

(b)

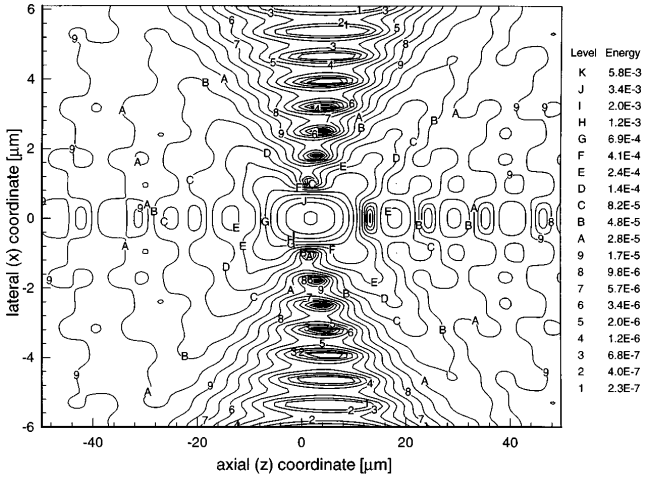

(c)

Fig. 6. Time-averaged electric energy density distributions in the $x-y$ meridional plane for a probe depth of 5 μm and for numerical apertures of (a) 0.3, (b) 0.6, and (c) 0.9. The calculations are for air ($n_1 = 1.0$) and silicon ($n_2 = 3.5$) and a wavelength of $\lambda = 1.3$ μm (infrared laser).

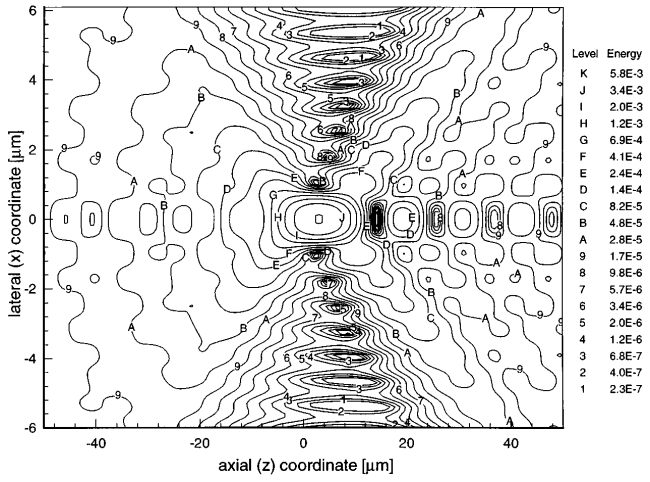

(a)

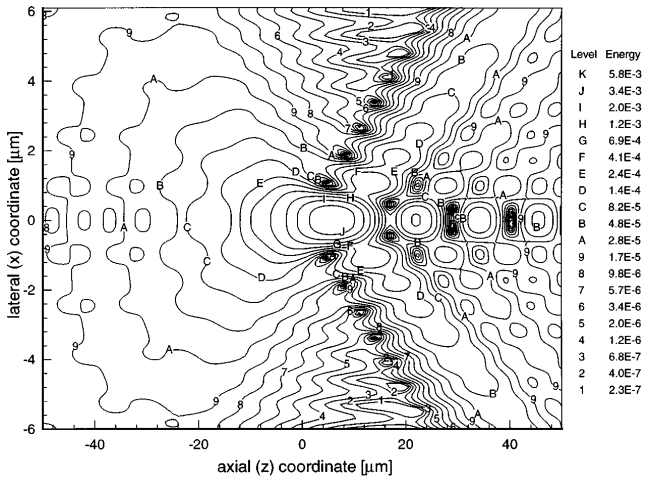

(b)

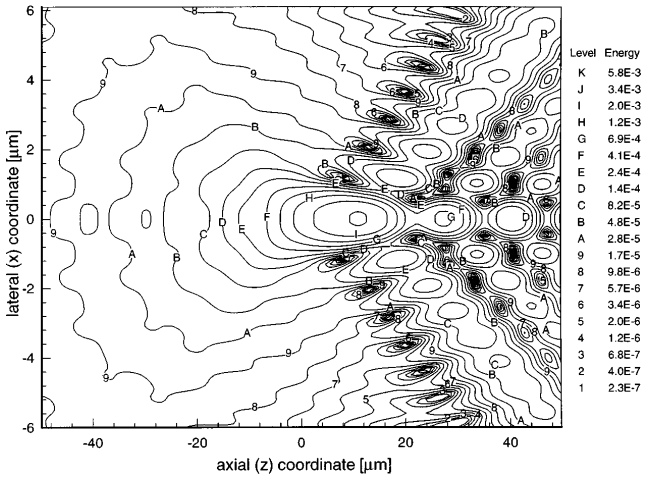

(c)

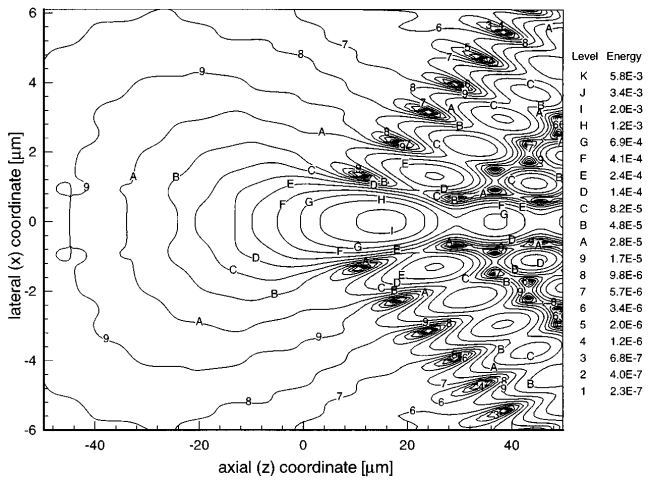

(d)

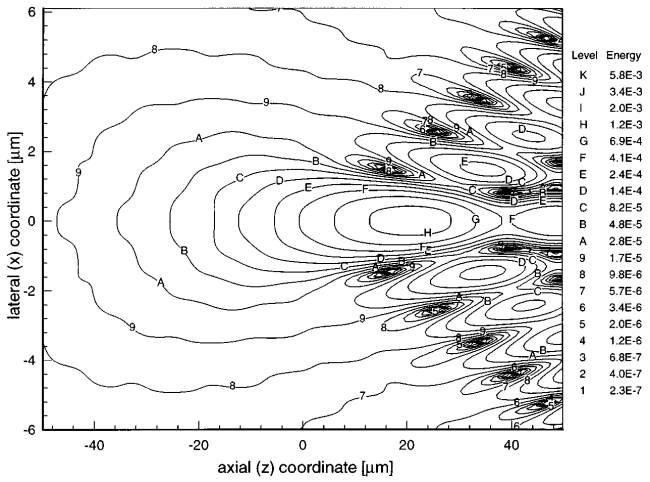

(e)

Fig. 7. Time-averaged electric energy density distributions in the $x-z$ meridional plane for a numerical aperture of 0.9 and for probe depths of (a) 10, (b) 20, (c) 40, (d) 80, and (e) 160 μm. The calculations are for air ($n_1 = 1.0$) and silicon ($n_2 = 3.5$) and a wavelength of $\lambda = 1.3$ μm (infrared laser).

direction than in the lateral direction, as can be seen from Fig. 3.

In Fig. 4 axial electric energy density line scans are plotted (horizontal axis) for probe depths of 10–280 μm (vertical axis). The gray levels are plotted on a linear scale, and so only the higher density regions are revealed. For a numerical aperture of 0.6 [Fig. 4(a)], on going from a probe depth of 0 to 120 μm, the energy density in the main maximum decreases by $\sim 4\times$. A secondary axial maximum in the positive z direction occurs at a depth of 120 μm. This maximum separates from the main maximum at 200 μm, where a third axial maximum occurs. For a numerical aperture of 0.9 [Fig. 4(b)] the effect of the probe depth is more pronounced than that for a numerical aperture of 0.6. On going from a probe depth of 0 to 120 μm, the energy density in the main maximum decreases by $\sim 6\times$, being initially higher and then lower than that for a numerical aperture of 0.6. Secondary and

third maxima in the positive z direction occur as the probe depth increases.

In Fig. 5 the electric energy density distribution in the focal $(x-y)$ plane (at the maximum of the energy density) is shown for a probe depth of 160 μm and a numerical aperture of 0.9. Compared with the well-known Airy distribution, the first minimum of the energy density distribution is increased, above zero, and the second and third maxima are also increased. The first and second minima occur at $x = 1.3$ and 3.1 μm, respectively, and the second maximum occurs at $x = 2.1$ μm. The corresponding values for the Airy disk in this case are 0.67, 1.17, and 0.87 μm, respectively. The distribution is slightly asymmetrical in the x and y directions.

B. Air–Silicon Interface

In this subsection all numerical computations were performed for a wavelength of $\lambda = 1.3$ μm and refractive indices of $n_1 = 1.0$ and $n_2 = 3.5$ for the first and the second material (silicon), respectively. In Figs. 6(a)–6(c) electric energy densities are shown in the $x-z$ plane for numerical apertures of (a) 0.3, (b) 0.6, and (c) 0.9, respectively, corresponding to solid semi-angles in silicon of 4.9°, 9.9°, and 14.9°, respectively. The probe depth is 5 μm. These energy densities for silicon show the same trends as those for glass of Fig. 2. However, the energy concentration is less, and the focus shift is larger. The ratio of the energy density in the main maximum for silicon and glass, corresponding to numerical apertures 0.3, 0.6, and 0.9, is in all three cases ~ 0.055. This small value is due partly to a worse energy concentration because of the smaller solid semi-angle in the silicon and partly to a larger amount of light reflected at the air–silicon interface.

For a numerical aperture of 0.3 the $x-z$ electric energy density distribution is closely symmetrical about the focal plane, and only a small focus shift occurs. No effect of interface focusing is apparent. For a numerical aperture of 0.6 the energy concentration is increased, and subsidiary axial minima and maxima occur. Comparison of the corresponding distributions for Figs. 2 and 6 shows that the relative energy densities at the subsidiary maxima are approximately the same for both air–glass and air–silicon focusing. For a numerical aperture of 0.9 the lateral and axial FWHM's of the main electric energy maximum are decreased, similar to the result of the corresponding case of air–glass, and the effect of interface focusing starts to dominate, with the subsidiary lateral maxima being shifted toward the positive axial direction. This asymmetry about the focal plane is more pronounced for the subsidiary axial maxima.

In Figs. 7(a)–7(e) electric energy densities are shown in the $x-z$ plane for a numerical aperture of 0.9 and probe depths of (a) 10, (b) 20, (c) 40, (d) 80, and (e) 160 μm. The energy density distributions follow the same trends as those for the corresponding distributions for air–glass of Fig. 3. The lateral subsidiary maxima are progressively shifted toward the positive axial direction.

Axial electric energy density scans are plotted as a function of probe depth for silicon in Figs. 8(a) and 8(b), corresponding to numerical apertures of 0.6 and 0.9, respectively. For a numerical aperture of 0.6 the energy density maximum is almost maintained for a probe depth range of 0–280 μm, the peak value decreasing by only $\sim 1.7\times$. Subsidiary axial peaks occur on both positive and negative sides of the main peak, with the positive peak being separated from the main peak at small probe depths. For a numerical aperture of 0.9 the energy density maximum decreases rapidly with increasing probe depth. For the probe depth range of 0–280 μm the maximum energy decreases by $\sim 6\times$. The focus shift is not a linear function of the probe depth, as is the case for a numerical aperture of 0.6. An axial subsidiary maximum occurs in the positive axial direction at a probe depth of ~ 40 μm, and this progressively becomes more separated from the main maximum as the probe depth increases.

The electric energy density distribution in the focal plane $(x-y)$ is shown in Fig. 9 for a probe depth of 160 μm and a numerical aperture of 0.9. The second maximum of the distribution is narrower, and the third maximum is $\sim 1.7\times$ higher, than those in the case of glass (Fig. 5). The distributions are only slightly asymmetrical about the optical axis, the effect being less than that for glass because of the smaller effective solid semi-angle in silicon.

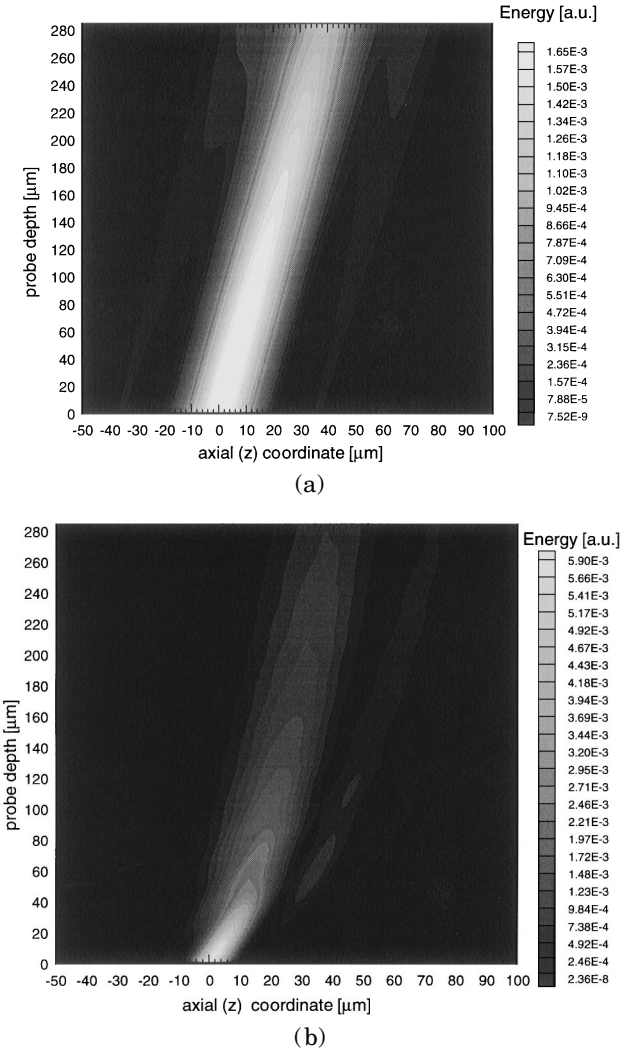

Fig. 8. Axial scans of the time-averaged electric energy density distribution for numerical apertures of (a) 0.6 and (b) 0.9 as a function of probe depth from 0 to 280 μm. The calculations are for air ($n_1 = 1.0$) and silicon ($n_2 = 3.5$) and a wavelength of $\lambda = 1.3$ μm (infrared laser).

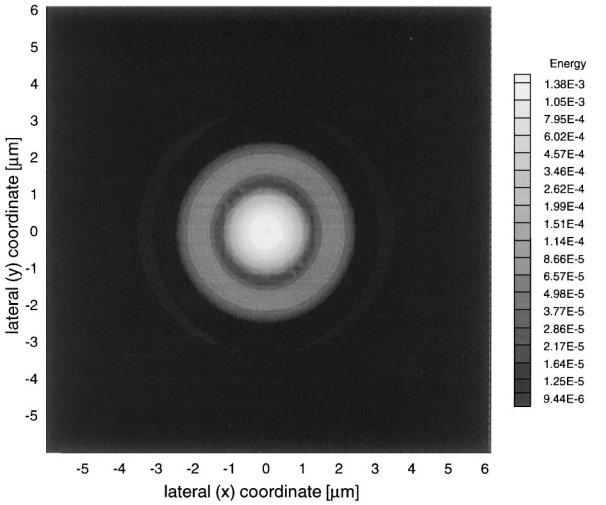

Fig. 9. Time-averaged electric energy density distribution for a numerical aperture of 0.9 in the focal $(x-y)$ plane when the probe depth is 160 μm. The calculations are for air ($n_1 = 1.0$) and silicon ($n_2 = 3.5$) and a wavelength of $\lambda = 1.3$ μm (infrared laser).

4. SUMMARY AND CONCLUSIONS

We previously obtained a rigorous mathematical solution for the diffraction occurring when light was focused by a lens without spherical aberration through a planar interface between materials of mismatched refractive indices, which produced spherical aberration. In the present work the diffraction integrals were transformed into a form that was computable. Time-averaged electric energy density distributions in the region of the focused probe were numerically evaluated for air–glass and air–silicon interfaces and a wide range of conditions, and consistent results were obtained.

The results showed that as the numerical aperture of the lens increased, the energy concentration increased and the size of the main maximum decreased. As either the probe depth or the refractive index of the second material increased, the opposite behavior occurred. As either the numerical aperture, the probe depth, or the refractive index of the second material increased, in general the focus shift of the main maximum increased and the energy distributions became asymmetrical, with the axial and lateral maxima moving in the positive z direction. Quantitative data for the electric energy densities, sizes, and positions of the energy maxima were obtained. The results showed, for example, that for a numerical aperture of 0.9, on going from a probe depth of 5 μm in glass to 160 μm in silicon, there was still a well-defined main maximum, but the axial width was increased $\sim 3.5\times$ and the electric energy density decreased by $\sim 4.5\times$.

The transformed diffraction integrals showed that the use of a lens without spherical aberration to focus into a second material was formally equivalent to the use of a lens with spherical aberration to focus into a single material. This constitutes a rigorous proof that the spherical aberration arising from focusing into a second material, for each particular depth, could be precisely compensated by the use of an additional correction lens that introduces an appropriate amount and sign of spherical aberration into the system.

ACKNOWLEDGMENTS

The authors thank D. G. Pettifor for provision of computing facilities in the Materials Modelling Laboratory of the Department of Materials, Oxford University, which was partially funded by Science and Engineering Research Council grant GR/H58278. P. Török thanks MEMC, Novara, Italy, for support, and P. Varga thanks the Hungarian Science Research Council for partial support on Foundation grant 2957. P. Török is on leave from the Central Research Institute for Physics, Hungarian Academy of Sciences.

*Present address, Multi-Imaging Centre, University of Cambridge, Downing Street, Cambridge CB2 3DY, UK.

REFERENCES AND NOTES

1. P. Török, P. Varga, Z. Laczik, and G. R. Booker, "Electromagnetic diffraction of light focused through a planar interface between materials of mismatched refractive indices: an integral representation," J. Opt. Soc. Am. A **12,** 325–332 (1995).
2. E. Wolf, "Electromagnetic diffraction in optical systems. I. An integral representation of the image field," Proc. R. Soc. London Ser. A **253,** 349–357 (1959).
3. B. Richards and E. Wolf, "Electromagnetic diffraction in optical systems. II. Structure of the image field in an aplanatic system," Proc. R. Soc. London Ser. A **253,** 358–379 (1959).
4. A. Boivin and E. Wolf, "Electromagnetic field in the neighbourhood of the focus of a coherent beam," Phys. Rev. B **138,** 1561–1565 (1965).
5. A. Hardy and D. Treves, "Structure of the electromagnetic field near the focus of a stigmatic lens," J. Opt. Soc. Am. **63,** 85–90 (1973).
6. H. H. Hopkins and M. J. Yzuel, "The computation of diffraction patterns in the presence of aberrations," Opt. Acta **17,** 157–182 (1970).
7. R. Kant, "Analytical solution of vector diffraction for focusing optical systems with Seidel aberrations. I. Spherical aberration, curvature of field, and distortion," J. Mod. Opt. **40,** 2293–2310 (1993).
8. H. Ling and S-W. Lee, "Focusing of electromagnetic waves through a dielectric interface," J. Opt. Soc. Am. A **1,** 965–973 (1984).
9. J. J. Stamnes, *Waves in Focal Regions,* 1st ed. (Adam Hilger, Bristol, UK, 1986).
10. P. Török, P. Varga, Z. Laczik, and G. R. Booker, "Electromagnetic diffraction of light focused through a planar interface between materials of mismatched refractive indices: an integral representation: errata," J. Opt. Soc. Am. A **12,** 1605 (1995).
11. It should be emphasized that this transformation is applicable only when the electric field is being computed inside the second material. When the diffraction integrals are applied to compute the field at the immediate vicinity of the interface and when $n_2 > n_1$, the application of this transformation excludes the evanescent waves from the expression, and thus for the latter case the original equations should be used.
12. M. R. Brozel, I. Grant, R. M. Ware, and D. J. Stirland, "Direct observation of the principal deep level (EL2) in undoped semi-insulating GaAs," Appl. Phys. Lett. **42,** 610–612 (1983).
13. G. R. Booker, Z. Laczik, and P. Kidd, "The scanning infrared microscope (SIRM) and its applications to bulk GaAs and Si: a review," Semicond. Sci. Technol. **7,** A110–A121 (1992).
14. P. Török, Z. Laczik, and G. R. Booker, "The development and use of a new confocal SIRM incorporating reflection, double-pass and phase contrast modes," Inst. Phys. Conf. Ser. **134,** 771–774 (1993).